Available online at www.sciencedirect.com
SCIENCE DIRECT®
European Journal of Mechanics B/Fluids 24 (2005) 751–766

Weakly nonlinear forced convection patterns in rectangular planform containers

A.A. Al-Ali [a], P.G. Daniels [b,*]

[a] *Department of Mathematics and Computer Science, Faculty of Science, UAE University, PO Box 15775, Al Ain, UAE*
[b] *Centre for Mathematical Science, City University, Northampton Square, London EC1V 0HB, UK*

Received 8 July 2004; received in revised form 14 January 2005; accepted 14 January 2005

Available online 15 April 2005

Abstract

This paper considers the structure of weakly nonlinear steady-state convection patterns in shallow rectangular planform containers heated from below. The lateral dimensions of the container are assumed to be much larger than the characteristic wavelength of convection, and the lateral boundaries are subject to forcing equivalent, for example, to imperfect thermal insulation in the Rayleigh–Benard problem. This has the effect of generating rolls parallel and perpendicular to the lateral boundaries. The resulting patterns are modelled by a coupled pair of nonlinear amplitude equations derived from a phenomenological model of convection introduced by Swift and Hohenberg [Phys. Rev. A15 (1977) 319]. These equations are applicable in the weakly nonlinear limit to a variety of pattern-forming systems such as the Rayleigh–Benard system. Solutions are found using both numerical and asymptotic methods. The boundary imperfection is shown to give rise to some novel effects, including the possibility of patterns containing square cells. More generally, patterns evolve that are dominated by rolls but with transitions to more complex bimodal forms near the edges of the container. The emergence and structure of transition lines, or grain boundaries, is analysed in detail.

1. Introduction

A common feature of experimental studies of Rayleigh–Benard convection is the presence of 'imperfections' which may arise typically through the geometry of the container or the thermal conditions imposed at the boundaries [1]. This can have important consequences for the motions that are observed. For example, imperfect thermal insulation of the sidewalls of a rectangular container leads to the replacement of the usual supercritical bifurcation from the conductive state by a smooth transition as the Rayleigh number is increased [2]. The same effect is also important in a wide variety of other problems, for example due to end effects in Taylor–Couette flow between rotating cylinders [3], in sloping convection [4] and in rotating convection [5]. The present paper is concerned with convection in a shallow rectangular container heated from below and considers how imperfections or forcing at the sidewalls affect the pattern of convection in the planform of the container. Previous solutions incorporating imperfect lateral boundaries are limited to planforms infinite in at least one direction, and the main objective of the present work is to obtain results for finite domains, as in experiments. In large planform systems it is generally difficult to obtain perfectly regular patterns in experiments. Forcing the system at the boundaries is of some interest experimentally because

* Corresponding author.
E-mail address: p.g.daniels@city.ac.uk (P.G. Daniels).

0997-7546/$ – see front matter
doi:10.1016/j.euromechflu.2005.01.004

when done in a controlled manner (see, for example, Pocheau and Croquette [6]) it offers a way of generating more regular behaviour, allowing closer comparison between theory and experiment.

Imperfections at a sidewall generate roll components parallel to that wall [7] so that for the general case where imperfections exist at all four sidewalls the solution must contain two orthogonal roll components. The interaction of these components is modelled here by a coupled pair of nonlinear amplitude equations. Solutions of this system in the perfect case [8] indicate an initial preference for rolls parallel to the shorter sides of the rectangle [9] and the subsequent emergence of perpendicular cross rolls near these boundaries [10] as the Rayleigh number is increased. This leads to the presence of transition lines, or grain boundaries, within the rectangle and the detailed structure and location of these were studied by Daniels and Lee [11]. Such boundaries, where patterns with different orientations meet in an abrupt fashion are important in crystal growth [12] and have been studied in the context of thermal convection by, for example, Manneville and Pomeau [13], Tesauro and Cross [14], Malomed et al. [15], Hari and Nepomnyashchy [16] and Hoyle [17].

The imperfections studied here are equivalent to the requirement that the amplitude functions of the two sets of orthogonal rolls assume non-zero values at the lateral boundaries of the rectangle: the amplitude equations and boundary conditions are formulated in Section 2 and can be derived in the weakly nonlinear limit from either the Oberbeck–Boussinesq equations governing Rayleigh–Benard convection or from simpler phenomenological models such as that introduced by Swift and Hohenberg [18]. Numerical results described in Section 3 focus on two cases, one where all four boundaries of the rectangle are subject to imperfections of equal magnitude and the other where just the shorter edges are subject to imperfections. In the first case an interesting sequence of two-dimensional patterns occurs as the Rayleigh number increases, including at one stage a pattern consisting of square cells. In the second case the emergence of cross rolls near the shorter edges occurs through a supercritical bifurcation of the stationary state which is analysed in Section 4. This results in the formation of grain boundaries which initially move away from the shorter edges of the rectangle but then approach again as the Rayleigh number increases. The location of the grain boundary as a function of both the Rayleigh number and the boundary forcing is determined in Section 5. The results are discussed in Section 6.

2. Formulation

The system of amplitude equations and boundary conditions to be studied here is generic in the sense that it can be derived in the weakly nonlinear limit from a number of nonlinear physical systems, including phenomenological models of convection discussed by Cross and Hohenberg [19] and the Oberbeck–Boussinesq equations governing Rayleigh–Benard convection (see below). A typical relaxational model widely studied in the literature is that introduced by Swift and Hohenberg [18]:

$$\frac{\partial \psi}{\partial t} = \epsilon\psi - (\nabla^2 + 1)^2\psi - \psi^3, \tag{1}$$

where ψ is a function of x, y and t, $\nabla^2 = \partial^2/\partial x^2 + \partial^2/\partial y^2$, x and y denote Cartesian coordinates and t denotes time. This equation contains the essential ingredients of diffusion and cubic nonlinearity which characterise the Oberbeck–Boussinesq system. The function ψ is a characteristic property of the flow, such as the vertical velocity component at the mid-plane level and ϵ is a parameter equivalent to the excess of the Rayleigh number above its critical value for an infinite layer. A finite domain $0 \leqslant x \leqslant L$, $0 \leqslant y \leqslant M$ is assumed where both L and M are large compared with unity. On the lateral boundaries it is assumed that

$$\psi = 4\lambda_{1,2}L^{-1}/\sqrt{3}, \quad \partial\psi/\partial x = 0 \quad \text{at } x = 0, L, \tag{2}$$

$$\psi = 4\gamma_{1,2}L^{-1}/\sqrt{3}, \quad \partial\psi/\partial y = 0 \quad \text{at } y = 0, M, \tag{3}$$

where $\lambda_{1,2}$ and $\gamma_{1,2}$ are finite imperfection parameters which in the Rayleigh–Benard system can represent, for instance, a small slip, displacement or thermal conductivity at the walls. Imperfections can also be introduced via non-zero values of the derivatives in (2), (3), with similar effect (see below).

Steady, spatially-periodic solutions of (1) exist for $\epsilon > 0$ and, for small values of $|\epsilon|$, amplitude equations describing orthogonal rolls aligned with the sidewalls are obtained by setting

$$\psi = \frac{2}{\sqrt{3}}L^{-1}\left\{A(X, Y, \tau)\,\mathrm{e}^{\mathrm{i}x} + B(X, Y, \tau)\,\mathrm{e}^{\mathrm{i}y}\right\} + c.c. + \cdots. \tag{4}$$

Here $c.c.$ denotes complex conjugate, A and B are complex functions representing the amplitudes of rolls with axes perpendicular to the x and y directions respectively (x-rolls and y-rolls) and X, Y and τ are defined by

$$x = LX, \quad y = LY, \quad t = L^2\tau/4. \tag{5}$$

It then follows from (1) that for finite values of

$$\delta = \epsilon L^2/4, \tag{6}$$

A and B satisfy the coupled pair of amplitude equations

$$\frac{\partial A}{\partial \tau} = \frac{\partial^2 A}{\partial X^2} + \delta A - A\big(|A|^2 + 2|B|^2\big), \tag{7}$$

$$\frac{\partial B}{\partial \tau} = \frac{\partial^2 B}{\partial Y^2} + \delta B - B\big(|B|^2 + 2|A|^2\big) \tag{8}$$

(see Daniels and Weinstein [8]). Finite values of δ are equivalent to an order L^{-2} band of values of ϵ near the critical value for an infinite layer, $\epsilon = 0$. Although the scalings (4)–(6) lead to the absence of Y and X derivatives in (7) and (8) respectively, both A and B will in general vary with both X and Y through the nonlinear interaction.

Boundary conditions for the system (7), (8) are derived from (2) and (3) by considering regions near each sidewall where x or y are of order unity. For the sidewall region near $x = 0$ the local solution for ψ satisfies $(\nabla^2 + 1)^2\psi = 0$ to leading order, allowing a solution for the x-roll component of the form $\psi \sim 2(\sqrt{3}L)^{-1}\,\mathrm{e}^{\mathrm{i}x}(a_1 + b_1 x) + c.c.$, where a_1 and b_1 are complex functions of Y and τ. However, matching with (4) requires that $b_1 = 0$ and the real and imaginary parts of a_1 $(= A(0, Y, \tau))$ are then fixed by the wall conditions (2). Further details for the case of an isolated wall are given by Daniels and Weinstein [20] and the extension to the present case leads to the four boundary conditions

$$A = \lambda_1 \quad \text{at } X = 0, \qquad A = \lambda_2\,\mathrm{e}^{-\mathrm{i}L} \quad \text{at } X = 1, \tag{9}$$

$$B = \gamma_1 \quad \text{at } Y = 0, \qquad B = \gamma_2\,\mathrm{e}^{-\mathrm{i}M} \quad \text{at } Y = a, \tag{10}$$

where $a = M/L$ is the aspect ratio of the rectangle. Note that if the derivatives of ψ in (2), (3) are non-zero, this simply generates additional (complex) terms on the right-hand sides of (9) and (10) – in either case the key effect of the imperfection is to generate non-zero boundary conditions for A and B. The absence of conditions on B at $X = 0, 1$ and A at $Y = 0, a$ is consistent with the form of Eqs. (7), (8); the necessary adjustments to accommodate the full boundary conditions (2), (3) are made within boundary layers of thickness x (or y) $\sim \epsilon^{-1/4} \sim L^{1/2}$ where fourth-order spatial derivatives enter the amplitude equations. These boundary layers are discussed by Brown and Stewartson [2] and Daniels and Weinstein [20] and are generally passive, allowing the amplitude and gradient in amplitude of the relevant component of (4) to reduce to zero at the boundary.

Rayleigh–Benard convection in a rectangular container with rigid horizontal boundaries is also governed (via suitable scale transformations from the physical variables) by Eqs. (7), (8) although in this case each of the coefficients of 2 in Eqs. (7), (8) is replaced by a Prandtl-number-dependent coefficient whose value varies from 1.23 for infinite Prandtl number to 14.3 for zero Prandtl number [21]. For this range of values no qualitative difference is expected in the behaviour of steady-state solutions compared with those of (7)–(10). Boundary conditions of the form (9), (10) correspond, for example, to sidewalls with imperfect thermal insulation; details of the derivation in the case of roll patterns between stress-free horizontal boundaries are given by Daniels [7] and in the case of rigid boundaries by Stewartson and Weinstein [22].

Solutions of (7)–(10) for the case $\lambda_{1,2} = \gamma_{1,2} = 0$ have been obtained by Daniels and Weinstein [8] and Daniels and Lee [11]; the present paper is concerned with non-zero values of the imperfection parameters.

3. Numerical results

Numerical solutions of the system (7)–(10) were obtained using a finite difference scheme based on central differences in X and Y and a forward difference in time. Steady-state solutions were allowed to evolve from an initial state

$$A = A_0(X, Y), \quad B = B_0(X, Y) \quad \text{at } \tau = 0 \tag{11}$$

and solutions were computed typically with step lengths $\Delta X = 0.0125$, $\Delta Y = 0.0125$ and $\Delta\tau = 0.00005$, the last of these being chosen sufficiently small to maintain numerical stability in the explicit scheme. Checks on accuracy were performed with other step sizes. For simplicity, solutions were found for cases in which A and B are real, corresponding to situations where L and M in (9) and (10) are integer multiples of 2π. Results are described here for two main cases, the first where all four imperfection parameters are equal and non-zero and the second where two of the imperfection parameters $(\lambda_{1,2})$ are equal and non-zero and the other two $(\gamma_{1,2})$ are zero. For definiteness the non-zero value is chosen to be 3 although other values give qualitatively similar results. If the values of the four parameters are non-zero but unequal the main effects caused by the loss of

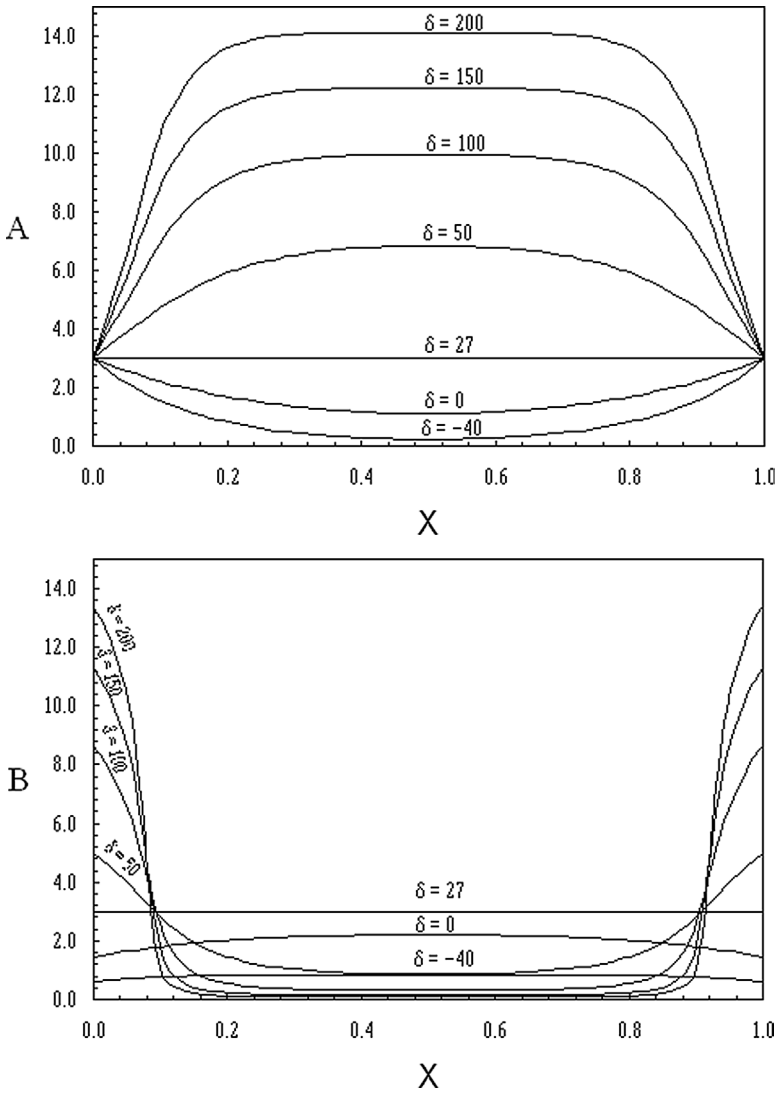

Fig. 1. Steady-state profiles A and B on $Y = 0.3$ for the case $a = 0.6$ with $\lambda_{1,2} = \gamma_{1,2} = 3$ and a range of values of δ.

symmetry are mostly confined to the edge regions of the rectangle as the control parameter δ increases and are not investigated in detail here.

Steady-state solutions for A and B in the first case were computed from the initial state

$$A_0 = 3 + \sin(\pi X), \qquad B_0 = 3 + \sin(\pi Y/a) \tag{12}$$

and results for several values of δ and an aspect ratio $a = 0.6$ are shown in Figs. 1 and 2. This value of a is chosen to allow comparison with previous results for the corresponding perfect problem by Daniels and Weinstein [8] and Daniels and Lee [11]. Other values of a give qualitatively similar results although the limiting cases of the square ($a = 1$) and channel ($a \to 0$) deserve special attention and are not discussed here. With A and B real, the Swift–Hohenberg function ψ can be approximated by the form

$$\psi = \frac{4}{\sqrt{3}} L^{-1}(A \cos x + B \cos y) \tag{13}$$

and contours of this function are shown in Fig. 3 for $L = 30\pi$, $M = 18\pi$.

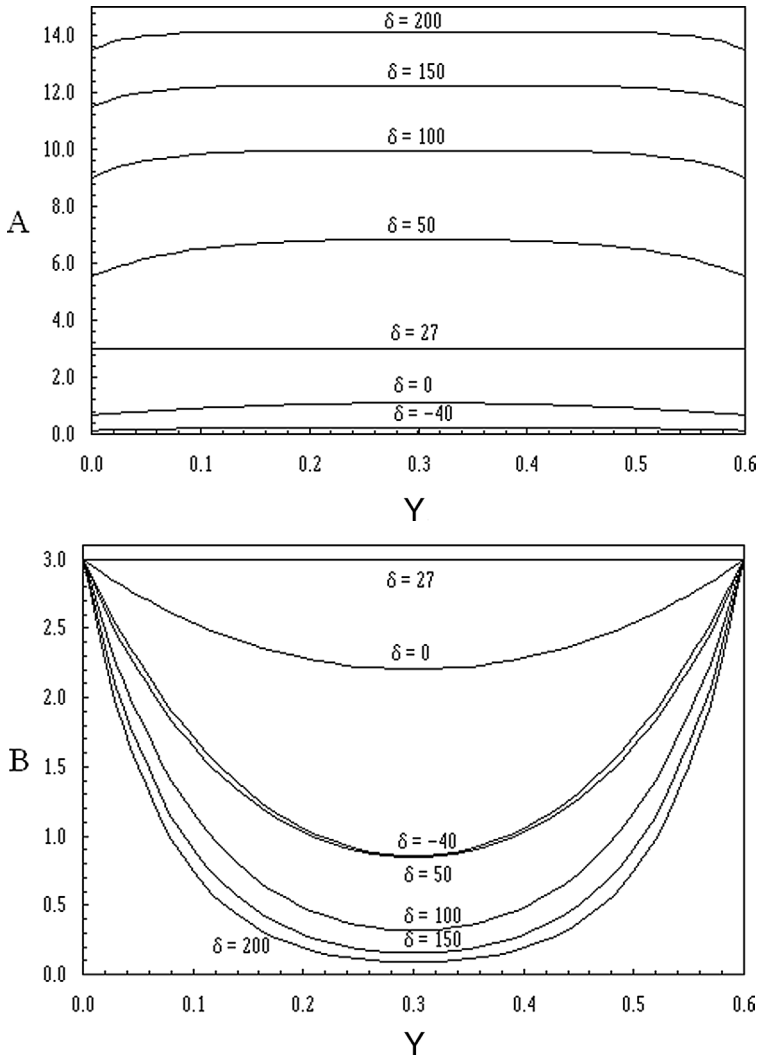

Fig. 2. Steady-state profiles A and B on $X = 0.5$ for the case $a = 0.6$ with $\lambda_{1,2} = \gamma_{1,2} = 3$ and a range of values of δ.

At large negative values of δ the steady-state solution approaches the form

$$A \sim \frac{3\cosh\{(-\delta)^{1/2}(X-1/2)\}}{\cosh\{(-\delta)^{1/2}/2\}}, \quad B \sim \frac{3\cosh\{(-\delta)^{1/2}(Y-a/2)\}}{\cosh\{(-\delta)^{1/2}a/2\}}, \quad -\delta \gg 1, \tag{14}$$

since the nonlinear terms in (7), (8) have a negligible effect on the solution, which is small except near the four walls of the rectangle. The pattern for $\delta = -40$ shown in Fig. 3 is interesting because although A and B are small throughout most of the rectangle they are of comparable magnitude. Thus the pattern is a bimodal mixture of x and y-rolls near the shorter ends but is dominated by y-rolls in the central region due to the closer proximity of the boundaries at $Y = 0, a$. As δ increases the steady-state magnitudes of A and B increase and at $\delta = 0$ there is a bimodal pattern throughout the rectangle. At $\delta = 27$ there is a solution with $A = B = 3$ throughout the rectangle, corresponding to a pattern of square cells oriented at 45 degrees to the walls. With further increase in δ the solution for A begins to dominate that for B throughout most of the rectangle. This is because at large δ the growth of A to the asymptotic core solution $A \sim \delta^{1/2}$ occurs when the core width $X = 1 \gg \delta^{-1/2}$ whereas the corresponding core solution $B \sim \delta^{1/2}$ can only occur when $Y = a \gg \delta^{-1/2}$. Since $a < 1$, the former occurs ahead of the latter as δ increases and so most of the domain is dominated by x-rolls when δ is large, with the value of B much less than that of A. This is confirmed by the solutions shown in Figs. 1–3 for $\delta \geqslant 50$ but there is also an indication of the existence of a bimodal state in which x and y-rolls coexist near the shorter lateral boundaries $X = 0$ and $X = 1$. This can be viewed as a manifestation

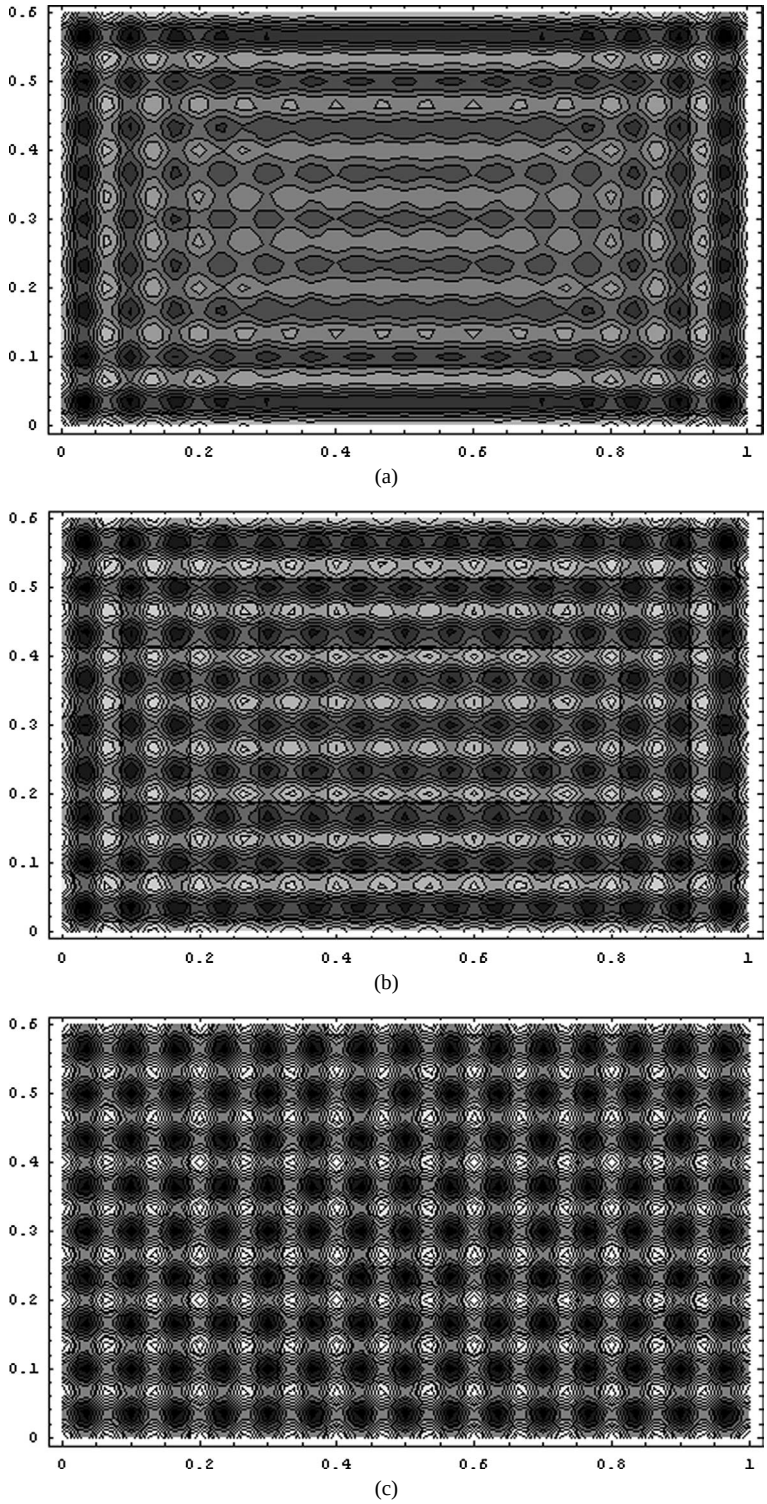

Fig. 3. Contours of the steady-state solution for ψ with $L = 30\pi$, $M = 18\pi$ and $a = 0.6$ for the case $\lambda_{1,2} = \gamma_{1,2} = 3$ with (a) $\delta = -40$, (b) $\delta = 0$, (c) $\delta = 27$, (d) $\delta = 50$, (e) $\delta = 100$.

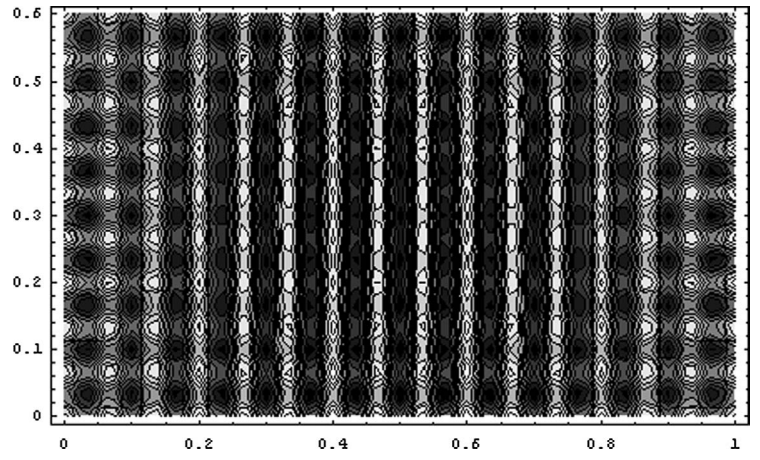

(d)

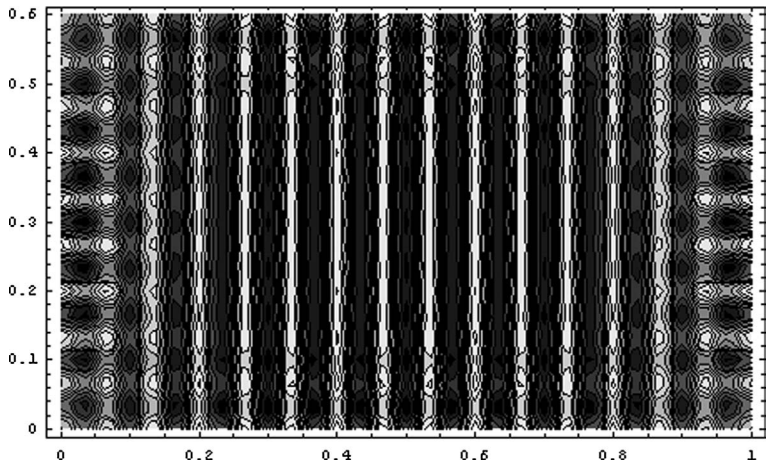

(e)

Fig. 3. Continued.

of the cross-roll instability discussed by Pomeau and Zaleski [10]: from Eq. (8) it is seen that y-roll perturbations of the form $B \sim e^{\sigma\tau}\sin(\pi Y/a)$ will grow on an x-roll state in any region where $|A|^2 < (\delta - \pi^2/a^2)/2$. In the present situation this first occurs near the ends $X = 0$ and $X = 1$ when

$$\delta > \delta_c = \frac{\pi^2}{a^2} + 2\lambda^2 \tag{15}$$

and in the case where $\lambda = \lambda_{1,2} = 3$ and $a = 0.6$ the critical value of δ is $\delta_c = 45.42$.

Results for the second case, where the two imperfection parameters γ_1 and γ_2 are set to zero and the initial state is taken as

$$A_0 = 3 + \sin(\pi X), \qquad B_0 = \sin(\pi Y/a), \tag{16}$$

are shown in Figs. 4 and 5, again for $a = 0.6$. Here the steady-state solution is dominated entirely by x-rolls until δ reaches the critical value $\delta_c = 45.42$ given by (15), at which point the primary steady-state solution consisting of x-rolls undergoes a bifurcation to a bimodal (x-roll/y-roll) state near the shorter lateral walls. Transition lines, or grain boundaries, separate these regions from the core region in which B is now identically zero, but in most respects the solution for $\delta = 100$ shown in Fig. 5 is qualitatively similar to that of the case where γ_1 and γ_2 are non-zero (Fig. 3). Strictly speaking, for the solution near $X = 0$, the transition line, $X = X_T$ say, can be defined by the largest value of X at which the steady linearized version of (8),

$$\frac{\partial^2 B}{\partial Y^2} + \left(\delta - 2|A|^2\right)B = 0, \tag{17}$$

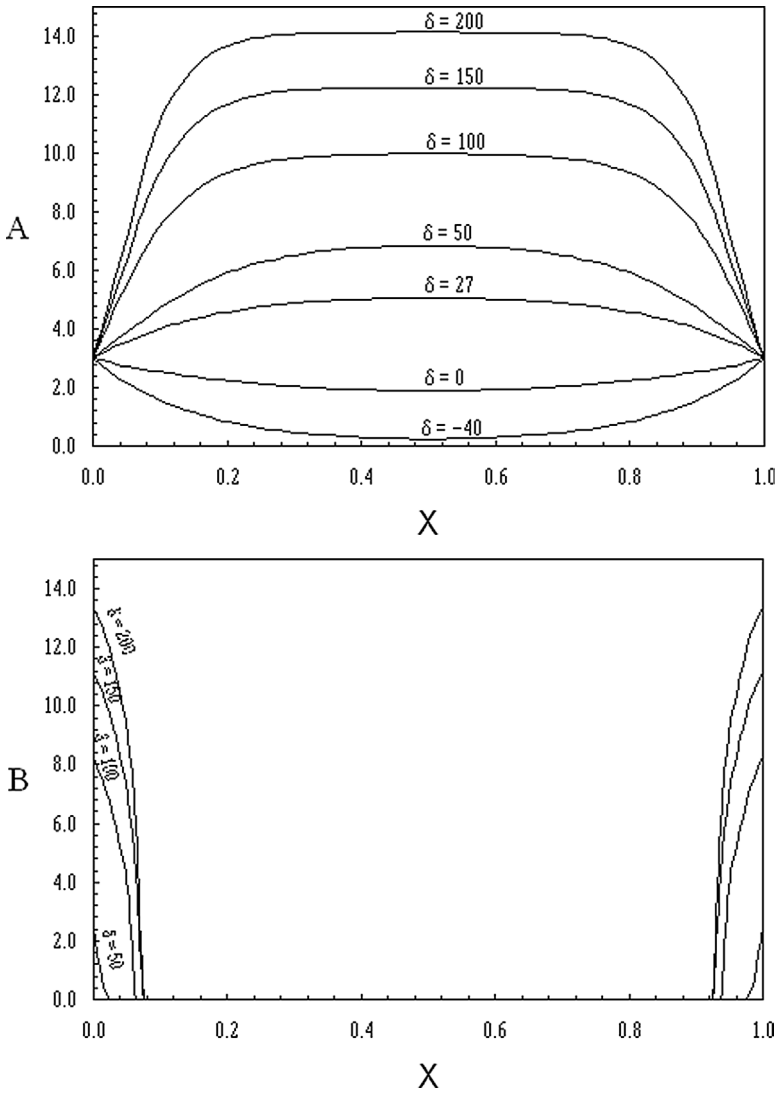

Fig. 4. Steady-state profiles A and B on $Y = 0.3$ for the case $a = 0.6$ with $\lambda_{1,2} = 3$, $\gamma_{1,2} = 0$ and a range of values of δ.

subject to $B = 0$ at $Y = 0$ and $Y = a$ has a non-trivial eigenfunction. If A is independent of Y then this corresponds to the condition $|A| = (\delta - \pi^2/a^2)^{1/2}/\sqrt{2}$. In practice, A is not independent of Y at X_T but this latter condition remains a good approximation for general values of δ and will be shown to be correct to leading order both as $\delta \to \delta_c$ and as $\delta \to \infty$. The bifurcation structure at δ_c and the solution structure as $\delta \to \infty$ are examined in more detail in the next two sections, in particular to determine the influence of the imperfection parameter λ on the position of the transition lines.

4. Bifurcation structure at $\delta = \delta_c$

For the symmetric case where $\gamma_1 = \gamma_2 = 0$, $\lambda_1 = \lambda_2 = \lambda > 0$ and A and B are real, the structure of the bifurcation at the critical value $\delta = \delta_c$ given by (15) can be analysed as follows. A symmetric steady-state solution of (7)–(10) for which $B = 0$ can be written in the form

$$A = A(X;\delta) = \left(\frac{2\delta m}{1+m}\right)^{1/2} \mathrm{sn}\left\{\frac{\delta^{1/2}(X-1/2)}{(1+m)^{1/2}} + K(m), m\right\}, \tag{18}$$

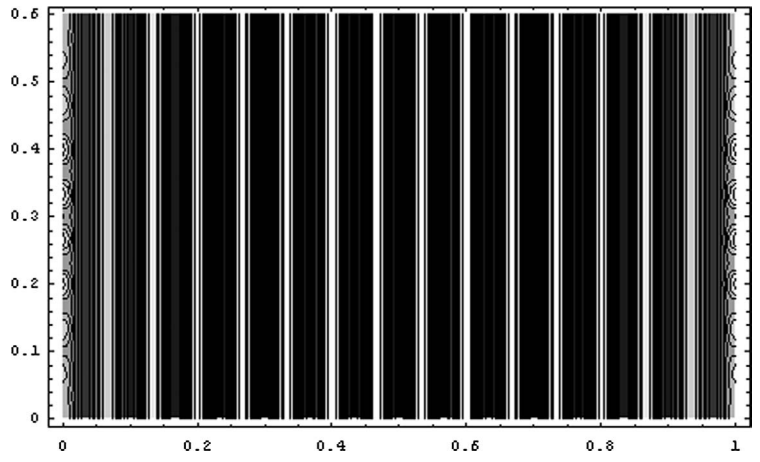

(a)

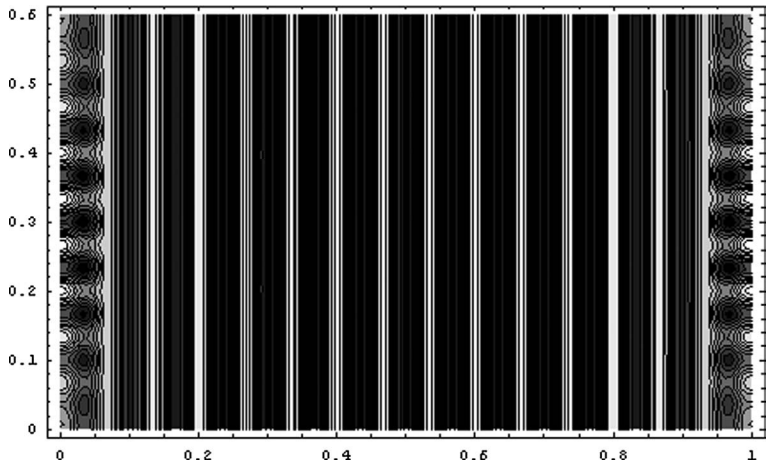

(b)

Fig. 5. Contours of the steady-state solution for ψ with $L = 30\pi$, $M = 18\pi$ and $a = 0.6$ for the case $\lambda_{1,2} = 3$, $\gamma_{1,2} = 0$ with (a) $\delta = 50$, (b) $\delta = 100$.

where sn is the Jacobian elliptic function (see, for example, Abramowitz and Stegun [23]), $K(m)$ is the complete elliptic integral of the first kind and the parameter m is fixed implicitly by the equations

$$\lambda = \left(\frac{2\delta m}{1+m}\right)^{1/2} \mathrm{sn}(\delta_m, m), \quad \delta_m = K(m) - \frac{\delta^{1/2}}{2(1+m)^{1/2}}. \tag{19}$$

When δ reaches the value δ_c this solution becomes unstable to cross-roll perturbations near $X = 0$ and $X = 1$ and a new stable steady-state solution can be found which locally consists of a combination of x-rolls and y-rolls.

Setting

$$\delta = \delta_c + \bar{\delta}, \tag{20}$$

the solution is found by assuming that $\bar{\delta} \ll 1$ and that the rectangular domain is subdivided into a core region $0 < X < 1, 0 \leqslant Y \leqslant a$ where $B = 0$ and

$$A = A_0 + \bar{\delta} A_1 + \bar{\delta}^2 A_2 + \bar{\delta}^3 A_3 + \cdots, \quad \bar{\delta} \to 0 \tag{21}$$

and wall regions near $X = 0$ and $X = 1$. The leading term A_0 satisfies the equation

$$\frac{\partial^2 A_0}{\partial X^2} + \left(\frac{\pi^2}{a^2} + 2\lambda^2\right) A_0 - A_0^3 = 0, \tag{22}$$

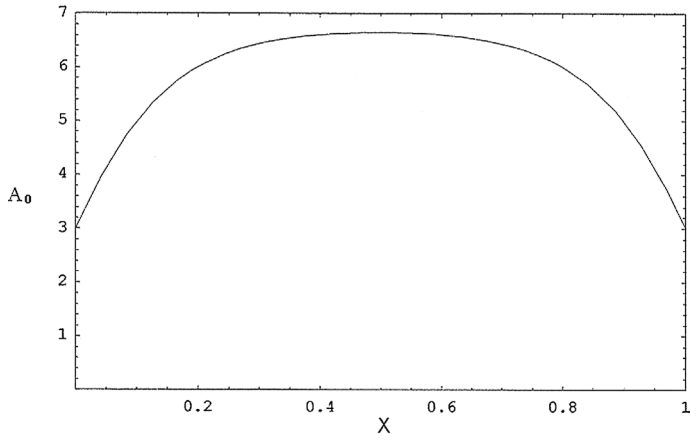

Fig. 6. The Jacobian elliptic function $A_0 = A(X;\delta_c)$ for the case $a = 0.6$, $\lambda = 3$, where $\delta_c = 45.42$.

with $A_0 = \lambda$ at $X = 0, 1$ and the solution is given by (18) evaluated at δ_c, $A_0 = A(X;\delta_c)$. This solution has the form

$$A_0 = \lambda + \mu_1 X + \mu_2 X^2 + \cdots, \quad X \to 0, \tag{23}$$

where

$$\mu_1 = \frac{\delta(2m)^{1/2}}{1+m}\,\mathrm{cn}(\delta_m, m)\,\mathrm{dn}(\delta_m, m), \qquad \mu_2 = -\frac{\lambda}{2}\left(\frac{\pi^2}{a^2} + \lambda^2\right), \tag{24}$$

and cn and dn are the Jacobian elliptic functions. The solution for A_0 in the case $a = 0.6, \lambda = 3$, where $m = 0.949$ and $\mu_1 = 25.74$ is shown in Fig. 6. Successive terms satisfy the equations

$$\frac{\partial^2 A_i}{\partial X^2} + \left(\frac{\pi^2}{a^2} + 2\lambda^2\right)A_i - 3A_0^2 A_i = \chi_i, \quad i = 1, 2, 3, \tag{25}$$

where $\chi_1 = -A_0$, $\chi_2 = 3A_0A_1^2 - A_1$ and $\chi_3 = 6A_0A_1A_2 - A_1^3 - A_2$. The solutions for A_1 and A_2 must vanish at $X = 0$ and $X = 1$ but the interaction between x-rolls and y-rolls in the wall regions forces A_3 to be non-zero at $X = 0$ and $X = 1$. This interaction is considered next.

In the wall region near $X = 0$, the solution is expressed in terms of a local coordinate $\overline{X}$ defined by

$$\overline{X} = \bar{\delta}^{-1} X \tag{26}$$

with

$$A = \lambda + \bar{\delta}\bar{A}_1 + \bar{\delta}^2\bar{A}_2 + \bar{\delta}^3\bar{A}_3 + \cdots, \tag{27}$$

$$B = \bar{\delta}^{1/2}\overline{B}_0 + \bar{\delta}^{3/2}\overline{B}_1 + \bar{\delta}^{5/2}\overline{B}_2 + \cdots, \tag{28}$$

where $\bar{A}_1, \ldots, \overline{B}_0, \ldots$ are functions of $\overline{X}$ and Y. Substitution into (7) shows that $\bar{A}_1$ is a linear function of $\overline{X}$ and the only solution which vanishes at $\overline{X} = 0$ and matches with (21) as $\overline{X} \to \infty$ is

$$\bar{A}_1 = \mu_1 \overline{X}. \tag{29}$$

From (8), $\overline{B}_0$ satisfies

$$\frac{\partial^2 \overline{B}_0}{\partial Y^2} + \frac{\pi^2}{a^2}\overline{B}_0 = 0; \qquad \overline{B}_0 = 0 \quad \text{at } Y = 0, a, \tag{30}$$

giving

$$\overline{B}_0 = b_0(\overline{X})\sin(\pi Y/a), \tag{31}$$

where b_0 is a function of $\overline{X}$ to be determined.

In (7), terms of order one, together with the boundary condition at $\overline{X} = 0$, give

$$\bar{A}_2 = \nu_1 \overline{X} + \mu_2 \overline{X}^2, \tag{32}$$

where $v_1 = \partial A_1/\partial X(0, Y)$. In (8), terms of order $\bar{\delta}^{3/2}$ give

$$\frac{\partial^2 \overline{B}_1}{\partial Y^2} + \frac{\pi^2}{a^2}\overline{B}_1 = \overline{B}_0(\overline{B}_0^2 + 4\lambda \bar{A}_1 - 1); \qquad \overline{B}_1 = 0 \quad \text{at } Y = 0, a. \tag{33}$$

This system has a solution only if

$$\int_0^a \overline{B}_0^2(\overline{B}_0^2 + 4\lambda \bar{A}_1 - 1)\,\mathrm{d}Y = 0, \tag{34}$$

which gives either $b_0 = 0$ or, for the positive root,

$$b_0 = \frac{2}{\sqrt{3}}(1 - 4\lambda\mu_1 \overline{X})^{1/2}, \quad \overline{X} < \overline{X}_T, \tag{35}$$

where $\overline{X}_T = (4\lambda\mu_1)^{-1}$. The only feasible solution for $\overline{X} > \overline{X}_T$ is $b_0 = 0$ and it is envisaged that for $\overline{X} < \overline{X}_T$ the solution (35) represents the stable steady-state form. Thus in the region near the wall $0 < \overline{X} < \overline{X}_T$, x-rolls and y-rolls coexist, while outside the transition line $\overline{X} = \overline{X}_T$ only x-rolls are present.

In (7), terms of order $\bar{\delta}$ give

$$\frac{\partial^2 \bar{A}_3}{\partial \overline{X}^2} = \bar{A}_1\left(\lambda^2 - \frac{\pi^2}{a^2}\right) + \lambda(2\overline{B}_0^2 - 1), \tag{36}$$

which shows that the solution for $\bar{A}_3$ is influenced by the presence of y-rolls. This equation must be integrated separately on each side of the transition line and this gives

$$\bar{A}_3 = -\frac{1}{2}\lambda\overline{X}^2 + \frac{1}{6}\mu_1\left(\lambda^2 - \frac{\pi^2}{a^2}\right)\overline{X}^3 + \frac{8}{3}\lambda\overline{X}^2\left(\frac{1}{2} - \frac{2}{3}\lambda\mu_1\overline{X}\right)\sin^2(\pi Y/a) + \overline{\omega}_1\overline{X} \tag{37}$$

for $\overline{X} < \overline{X}_T$, having made use of the fact that $\bar{A}_3 = 0$ at $\overline{X} = 0$, and

$$\bar{A}_3 = -\frac{1}{2}\lambda\overline{X}^2 + \frac{1}{6}\mu_1\left(\lambda^2 - \frac{\pi^2}{a^2}\right)\overline{X}^3 + \omega_1\overline{X} + \omega, \quad \overline{X} > \overline{X}_T, \tag{38}$$

where ω is an arbitrary function of Y and, from matching with the core solution, $\omega_1 = \partial A_2/\partial X(0, Y)$. Continuity of $\bar{A}_3$ and $\partial\bar{A}_3/\partial\overline{X}$ at $\overline{X} = \overline{X}_T$ now gives

$$\bar{\omega}_1 = \omega_1 - \frac{1}{3\mu_1}\sin^2(\pi Y/a) \tag{39}$$

and

$$\omega = -\frac{1}{36\lambda\mu_1^2}\sin^2(\pi Y/a). \tag{40}$$

The solution for $\bar{A}_3$ is of interest because it shows how the amplitude of x-rolls varies with Y throughout the wall region and that this variation extends, via the solution for ω above, into the region outside the transition line. This variation in turn influences the core solution through the matching condition

$$A_3(0, Y) = \omega \tag{41}$$

which provides one boundary condition for the outer function $A_3(X, Y)$. By symmetry, the other boundary condition is

$$A_3(1, Y) = \omega \tag{42}$$

and it follows that there is an order $\bar{\delta}^3$ variation with Y in the amplitude of the main x-roll pattern throughout the container, associated with the outer term A_3. In fact, the conditions (41), (42) can be simply viewed as a Y-dependent correction to λ, and the core solution (21) to terms of order $\bar{\delta}^3$ is just the exact solution (18), (19) with δ replaced by (20) and λ replaced by

$$\lambda - \frac{\bar{\delta}^3}{36\lambda\mu_1^2}\sin^2(\pi Y/a) \tag{43}$$

in (19). Thus the effect of the y-rolls near the boundaries is equivalent to a small, y-dependent reduction in the value of the imperfection parameter, with the maximum effect occurring at the centre-line $Y = a/2$.

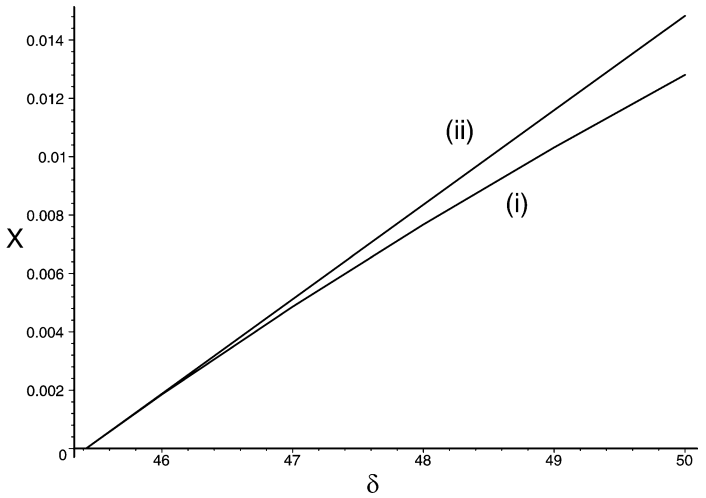

Fig. 7. Comparison of the transition line position X calculated (i) numerically from the steady-state solution using $A(X, a/2) = (\delta - \pi^2/a^2)^{1/2}/\sqrt{2}$ and (ii) from the asymptotic result (44), for the case $a = 0.6$, $\lambda = 3$.

In summary, it has been shown that when δ just exceeds δ_c, the stable steady-state solution will contain transition lines located at $X = X_T$ and $X = 1 - X_T$ where

$$X_T \sim (4\lambda\mu_1)^{-1}(\delta - \delta_c), \quad \delta \to \delta_c + . \tag{44}$$

Within the transition line near $X = 0$ the amplitude of y-rolls (assuming the positive solution for B) is given by

$$B \sim 4(\lambda\mu_1/3)^{1/2}(X_T - X)^{1/2}\sin(\pi Y/a), \quad X < X_T. \tag{45}$$

The result (44) is compared with the numerical computations of Section 3 in Fig. 7 and indicates good agreement. Note also that as $\lambda \to 0$, μ_1 remains finite and non-zero so that $X_T \to \infty$ in (44). Thus the distance of the transition line from the wall increases as the imperfection tends to zero; consideration of the case $\lambda = 0$ [8] shows that the transition line is then located at $X_T \sim (\delta - \delta_c)^{1/2}(\sqrt{2}\mu_1)^{-1}$.

5. Solution structure as $\delta \to \infty$

Again the symmetric case where $\lambda_1 = \lambda_2 = \lambda > 0$, $\gamma_1 = \gamma_2 = 0$ and A and B are real is considered. The structure of the steady-state asymptotic solution in the limit as $\delta \to \infty$ is similar to that of the perfect case described by Daniels and Lee [11]. The solution for B is assumed to reach exponentially small values along a path

$$X \sim \delta^{-1/2}U(Y), \tag{46}$$

where U is a function of Y to be determined below. This implies that the *effective* transition line is located at $X = \delta^{-1/2}U(Y)$ rather than at $X = X_T$, the solution of (17). With $X_T = \delta^{-1/2}U(a/2)$, the solution for B bifurcates from zero at $X = X_T$ but remains exponentially small in the region $\delta^{-1/2}U(Y) < X < X_T$. The bifurcation at X_T is 'local' in the sense that the eigenfunction of (17) is non-exponentially small only in the immediate neighbourhood of $Y = a/2$, where U has a maximum value. Either side of the line (46), A and B can be expanded as

$$A = \delta^{1/2}\tilde{A}_0(s, Y) + \delta^{-1/2}\tilde{A}_1(s, Y) + \cdots, \tag{47}$$

$$B = \delta^{1/2}\widetilde{B}_0(s, Y) + \cdots, \tag{48}$$

where $s = \delta^{1/2}X - U(Y)$ and with B identically zero for $s > 0$. It is found that

$$\tilde{A}_0 = \tanh\{(s + c)/\sqrt{2}\}, \quad s > 0, \tag{49}$$

where $c = \sqrt{2}\tanh^{-1}(1/\sqrt{2})$ and that

$$\tilde{A}_0 = \sqrt{2/3}\,\mathrm{sech}(d - s), \quad \widetilde{B}_0^2 = 1 - 2\tilde{A}_0^2, \quad s < 0, \tag{50}$$

where $d = \ln\sqrt{3}$. Consideration of the term $\tilde{A}_1$ then shows that

$$A \sim \delta^{1/2}\left\{\frac{2\sqrt{2}}{\sqrt{3}}\,\mathrm{e}^{s} + \cdots\right\} - \delta^{-1/2}\left\{\frac{d_2}{2\sqrt{2}}\,\mathrm{e}^{-s} + \cdots\right\} + \cdots, \tag{51}$$

as $s \to -\infty$, where d_2 is a function of Y given by

$$8d_2 = U''\big(2\ln|U'| - \ln\delta - k_2\big), \tag{52}$$

and k_2 is a finite constant. The result (52) is obtained by matching across a transition layer centred on (46) where s is of order $\delta^{-1/3}$. Within this region the amplitude of x-rolls reaches the value $A = (\delta - \pi^2/a^2)^{1/2}/\sqrt{2}$. The behaviour (51) must match with the solution in a wall region where the local coordinate $\widetilde{X}$ is defined by $X = \delta^{-1/2}\widetilde{X}$ and, assuming the positive solution for B,

$$A = \tilde{A}(\widetilde{X}, Y) + \cdots, \quad B = \delta^{1/2} + \cdots, \quad \delta \to \infty. \tag{53}$$

From (7), the function $\tilde{A}$ satisfies

$$\frac{\partial^2\tilde{A}}{\partial\widetilde{X}^2} - \tilde{A} = 0 \tag{54}$$

and since $\tilde{A} = \lambda$ on $\widetilde{X} = 0$ it follows that

$$\tilde{A} = \lambda\cosh\widetilde{X} + G(Y)\sinh\widetilde{X}, \tag{55}$$

where G is an arbitrary function of Y. Since $\widetilde{X} = s + U$, matching with (51) as $\widetilde{X} \to \infty$ implies that

$$G = \frac{4\sqrt{2}}{3}\delta^{1/2}\,\mathrm{e}^{-U} - \lambda = \frac{d_2}{\sqrt{2}}\delta^{-1/2}\,\mathrm{e}^{U} + \lambda \tag{56}$$

and substitution for d_2 from (52) implies that U must be found by solving the equation

$$U''\big(2\ln|U'| - \ln\delta - k_2\big) = 64\delta\,\mathrm{e}^{-2U}/3 - 16\sqrt{2}\delta^{1/2}\lambda\,\mathrm{e}^{-U}. \tag{57}$$

The imperfection parameter λ generates an additional term on the right-hand side, compared with the corresponding result for $\lambda = 0$ obtained by Daniels and Lee [11].

Eq. (57) is now solved in the limit $\delta \to \infty$ by writing

$$U = \frac{1}{2}\ln\delta - \frac{1}{2}\ln(\ln\delta) + P(Y), \tag{58}$$

in which case $P(Y)$ satisfies

$$P'' + \frac{64}{3}\,\mathrm{e}^{-2P} = (\ln\delta)^{-1/2}F(P, P', P''), \tag{59}$$

where

$$F(P, P', P'') = 16\sqrt{2}\lambda\,\mathrm{e}^{-P} + (\ln\delta)^{-1/2}P''\big(2\ln|P'| - k_2\big). \tag{60}$$

This suggests that P can be expanded in inverse powers of $(\ln\delta)^{1/2}$,

$$P = P_0(Y) + (\ln\delta)^{-1/2}P_1(Y) + \mathrm{O}\big((\ln\delta)^{-1}\big), \tag{61}$$

where the leading term P_0 satisfies the equation

$$P_0'' + \frac{64}{3}\,\mathrm{e}^{-2P_0} = 0. \tag{62}$$

The relevant solution is the one that is symmetric about $Y = a/2$ and has singular behaviour $P_0 \to -\infty$ that coincides with the sides of the rectangle $Y = 0$ and $Y = a$, giving

$$P_0 = \ln\left\{\frac{8a}{\sqrt{3}\pi}\sin(\pi Y/a)\right\}. \tag{63}$$

This ensures that the transition line bends into the corners of the rectangle, allowing consistent solutions to be found there [11].

The imperfection λ generates the next term P_1 which satisfies the equation

$$P_1'' - \frac{128}{3}\,\mathrm{e}^{-2P_0}P_1 = 16\sqrt{2}\lambda\,\mathrm{e}^{-P_0}. \tag{64}$$

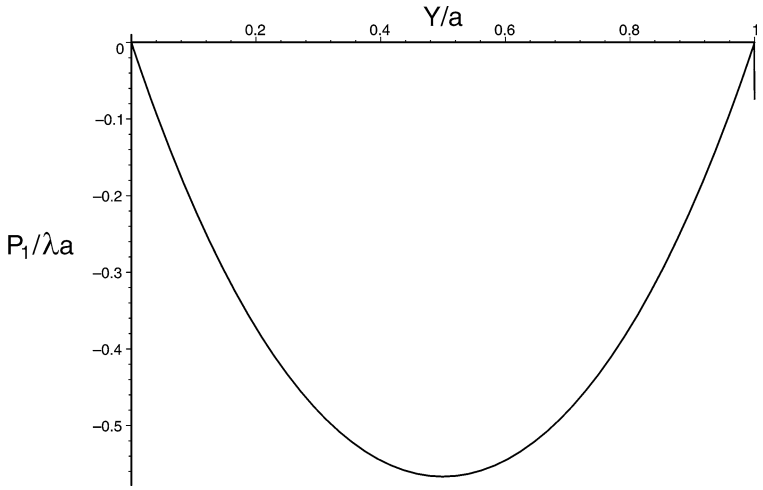

Fig. 8. The imperfection function $P_1/\lambda a$.

Using (63), this is found to have general solution

$$P_1 = C\left(\frac{a}{\pi} - Y\cot(\pi Y/a)\right) + D\cot(\pi Y/a) - \frac{2\sqrt{6}\lambda a}{\pi}\operatorname{cosec}(\pi Y/a), \tag{65}$$

where C and D are arbitrary constants. These must be chosen to ensure that the solution is symmetric about $Y = a/2$ and to avoid algebraic growth as $Y \to 0$ and $Y \to a$, which would be too large to match with the corner regions described by Daniels and Lee [11]. This gives

$$P_1 = \frac{4\sqrt{6}\lambda a}{\pi^2}\left\{1 - \frac{\pi}{2}\operatorname{cosec}(\pi Y/a) - \pi\left(\frac{Y}{a} - \frac{1}{2}\right)\cot(\pi Y/a)\right\} \tag{66}$$

and is shown in Fig. 8.

The solution for P_1 determines the correction to the position of the transition line, or grain boundary, due to the presence of the imperfection. From (46), (58) and (61) the transition line is located at

$$\begin{aligned} X = {} & \delta^{-1/2}\left\{\frac{1}{2}\ln\delta - \frac{1}{2}\ln(\ln\delta) + \ln\left(\frac{8a}{\sqrt{3}\pi}\sin(\pi Y/a)\right)\right\} \\ & + \delta^{-1/2}(\ln\delta)^{-1/2}\frac{4\sqrt{6}\lambda a}{\pi^2}\left\{1 - \frac{\pi}{2}\operatorname{cosec}(\pi Y/a) - \pi\left(\frac{Y}{a} - \frac{1}{2}\right)\cot(\pi Y/a)\right\} \\ & + \mathrm{O}\left(\delta^{-1/2}(\ln\delta)^{-1}\right) \end{aligned} \tag{67}$$

as $\delta \to \infty$. Fig. 9 shows a comparison between this formula evaluated at $Y = a/2$ with $\lambda = 3$ and $a = 0.6$ and the numerical computations of Section 3 for values of δ up to 600. In the latter case, the results show the value of X at which $A = (\delta - \pi^2/a^2)^{1/2}/\sqrt{2}$ and $Y = a/2$ interpolated from the relevant steady-state solution. This indicates good agreement and shows that the transition line approaches the wall as $\delta \to \infty$. The curve computed numerically by Daniels and Lee [11] for the case $\lambda = 0$ is also shown in Fig. 9 for comparison. The main effect of the imperfection in (67) is to move the transition line closer to the wall than in the case $\lambda = 0$. In this respect, the imperfection has a similar effect to that observed in the post-bifurcation region $\delta = \delta_c+$ discussed in Section 4.

6. Discussion

Numerical and asymptotic solutions have been found describing the effect of imperfect lateral boundary conditions on the structure of orthogonal roll patterns in a rectangular geometry. Solutions of the coupled pair of amplitude equations derived from the weakly nonlinear limit of the Swift–Hohenberg equation studied here are also relevant to the Rayleigh–Benard problem between rigid boundaries for a specific Prandtl number [21] and for general Prandtl numbers in a qualitative sense. Various simplifications have been made in order to bring out the main features of the solution, and it would be an interesting extension

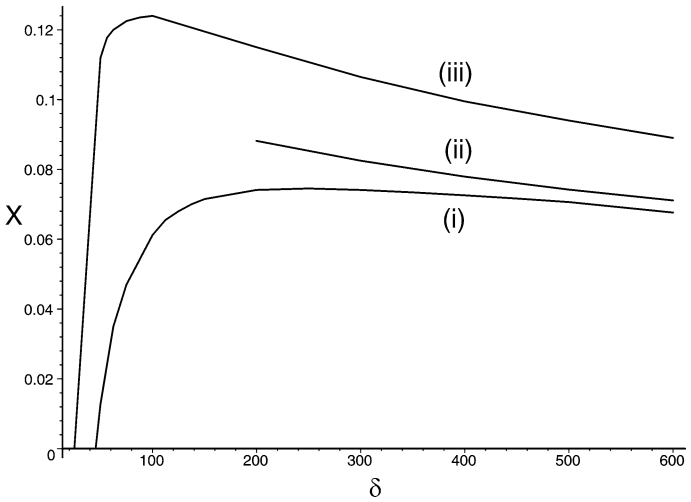

Fig. 9. Comparison of the transition line position X calculated (i) numerically from the steady-state solution using $A(X, a/2) = (\delta - \pi^2/a^2)^{1/2}/\sqrt{2}$ and (ii) from the asymptotic formula (67) with $Y = a/2$, for the case $a = 0.6$, $\lambda = 3$. The corresponding numerical result (iii) for the case $a = 0.6$, $\lambda = 0$ obtained by Daniels and Lee [11] is also shown.

of the present work to consider cases where L and M are not integer multiples of 2π and other more general forms of (9), (10) where A and B are complex functions of X and Y. It is known [24] that boundary forcing is one mechanism for the generation of phase-winding solutions in which the arguments of the complex amplitudes A and B vary with X and Y respectively. Such solutions correspond to changes in wavelength and thus the possibility of fitting different numbers of rolls into the container. Transitions between such solutions with different numbers of rolls may arise as secondary instabilities or through nonlinear fold bifurcations. By restricting attention to real values of A and B, such transitions are excluded from the present study.

Two different combinations of imperfection parameters have been studied in detail, the first corresponding to equal imperfections on all of the lateral walls ($\lambda_{1,2} = \gamma_{1,2} = 3$). At moderate values of the control parameter δ such imperfections have a significant impact and generally produce bimodal patterns throughout the rectangle. At higher values of δ the imperfections on the longer walls ($\gamma_{1,2}$) have relatively little impact on the convection pattern, except very close to these walls. The imperfections on the shorter walls ($\lambda_{1,2}$) control the growth of bimodal patterns near these walls which occur via a supercritical bifurcation in the case when $\gamma_{1,2} = 0$. Non-zero values of γ_1 and γ_2 generally result in the replacement of the bifurcation by a smooth transition as the control parameter increases, but the emerging supercritical state is not significantly different from that studied in Section 4 apart from the fact that it has no distinct transition lines. When $\gamma_{1,2} = 0$, the imperfections on the shorter walls ($\lambda_{1,2}$) shift the location of the transition lines nearer to the walls than in the case of no imperfection. For a *fixed* size of (small) imperfection, the bifurcation criterion (15) is always reached as the control parameter increases but if the size of the imperfection is such that $|\lambda_{1,2}| > (\delta - \pi^2/a^2)^{1/2}/\sqrt{2}$ then the criterion (15) is never met and the cross-rolls are not generated at all.

The present work is confined to roll patterns orthogonal to the boundaries of the rectangle and these are precisely the roll components that are generated by the imperfection at the boundaries. In practice, it is likely that other modes of convection may also be significant in the same range of control parameter ($-\infty < \delta < \infty$) such as the diagonal modes discussed by Daniels [25] and observed in numerical simulations of the Swift–Hohenberg equation by Greenside and Coughran [26]. The interaction of such modes with those considered here is left for future consideration.

References

[1] E.L. Koschmieder, Benard Cells and Taylor Vortices, Cambridge University Press, 1993.
[2] S.N. Brown, K. Stewartson, On thermal convection in a large box, Stud. Appl. Math. 57 (1977) 187.
[3] I.C. Walton, The transition to Taylor vortices in a closed rapidly rotating cylindrical annulus, Proc. Roy. Soc. London Ser. A 372 (1980) 201.
[4] P.G. Daniels, The onset of Benard convection in a shallow sloping container, Quart. J. Mech. Appl. Math. 35 (1982) 49.
[5] P.G. Daniels, The effect of centrifugal acceleration on axisymmetric convection in a shallow rotating cylinder or annulus, J. Fluid Mech. 99 (1980) 65.
[6] A. Pocheau, V. Croquette, Dislocation motion: a wavenumber selection mechanism in Rayleigh–Benard convection, J. Physique 45 (1984) 35.

[7] P.G. Daniels, The effect of distant sidewalls on the transition to finite amplitude Benard convection, Proc. Roy. Soc. London Ser. A 358 (1977) 173.
[8] P.G. Daniels, M. Weinstein, On finite-amplitude patterns of convection in a rectangular-planform container, J. Fluid Mech. 317 (1996) 111.
[9] S.H. Davis, Convection in a box: linear theory, J. Fluid Mech. 30 (1967) 465.
[10] Y. Pomeau, S. Zaleski, Wavelength selection in one-dimensional cellular structures, J. Physique 42 (1981) 515.
[11] P.G. Daniels, A.T. Lee, On the boundary-layer structure of patterns of convection in rectangular-planform containers, J. Fluid Mech. 393 (1999) 357.
[12] J. Friedel, Dislocations, Addison-Wesley, 1964.
[13] P. Manneville, Y. Pomeau, A grain boundary in cellular structures near the onset of convection, Philos. Mag. A 48 (1983) 607.
[14] G. Tesauro, M.C. Cross, Grain boundaries in models of convective patterns, Philos. Mag. A 56 (1987) 703.
[15] B.A. Malomed, A.A. Nepomnyashchy, M.I. Tribelsky, Domain boundaries in convection patterns, Phys. Rev. A 42 (1990) 7244.
[16] A. Hari, A.A. Nepomnyashchy, Dynamics of curved domain boundaries in convection patterns, Phys. Rev. E 50 (1994) 1661.
[17] R.B. Hoyle, Steady squares and hexagons on a subcritical ramp, Phys. Rev. E 51 (1995) 310.
[18] J.B. Swift, P.C. Hohenberg, Hydrodynamic fluctuations at the convective instability, Phys. Rev. A 15 (1977) 319.
[19] M.C. Cross, P.C. Hohenberg, Pattern formation outside of equilibrium, Rev. Mod. Phys. 65 (1993) 851.
[20] P.G. Daniels, M. Weinstein, On finite-amplitude patterns of convection near a lateral boundary, Quart. J. Mech. Appl. Math. 45 (1992) 315.
[21] V.R. Ferguson, P.G. Daniels, Convection patterns near a lateral boundary, IMA J. Appl. Math. 67 (2002) 99.
[22] K. Stewartson, M. Weinstein, Marginal convection in a large rigid box, Phys. Fluids 22 (1979) 1421.
[23] M. Abramowitz, I.A. Stegun, Handbook of Mathematical Functions, Dover, 1965.
[24] M.C. Cross, P.G. Daniels, P.C. Hohenberg, E.D. Siggia, Effect of distant sidewalls on wavenumber selection in Rayleigh–Benard convection, Phys. Rev. Lett. 45 (1980) 898.
[25] P.G. Daniels, Onset of convection in shallow cylindrical containers, Proc. Roy. Soc. London Ser. A 456 (2000) 527.
[26] H.S. Greenside, W.M. Coughran, Nonlinear pattern formation near the onset of Rayleigh–Benard convection, Phys. Rev. A 30 (1984) 398.